Neurobiology of Disease 54 (2013) 169–182

Contents lists available at SciVerse ScienceDirect

Neurobiology of Disease

journal homepage: www.elsevier.com/locate/ynbdi

Fast motor axon loss in SMARD1 does not correspond to morphological and functional alterations of the NMJ

Frank Krieger [a], Nicole Elflein [a], Rocio Ruiz [c], Joana Guerra [d], Antonio L. Serrano [d], Esther Asan [b], Lucia Tabares [c], Sibylle Jablonka [a,*]

[a] Institute for Clinical Neurobiology, University of Wuerzburg, Josef-Schneider-Str. 11, 97080 Wuerzburg, Germany
[b] Institute for Anatomy and Cell Biology, University of Wuerzburg, Koellikerstr. 6, 97070 Wuerzburg, Germany
[c] Department of Medical Physiology and Biophysics, School of Medicine, University of Seville, 41009 Seville, Spain
[d] Cell Biology Group, Department of Experimental and Health Sciences, Pompeu Fabra University (UPF), CIBER on Neurodegenerative diseases (CIBERNED); 08003 Barcelona, Spain

ARTICLE INFO

Article history:
Received 16 September 2012
Revised 30 November 2012
Accepted 21 December 2012
Available online 4 January 2013

Keywords:
SMARD1
Nmd^{2J} mouse
Motor axon
Neuromuscular junction
Neurotransmission

ABSTRACT

Spinal muscular atrophy with respiratory distress type 1 (SMARD1) is a childhood motoneuron disease caused by mutations in the gene encoding for IGHMBP2, an ATPase/Helicase. Paralysis of the diaphragm is an early and prominent clinical sign resulting both from denervation and myopathy. In skeletal muscles, muscle atrophy mainly results from loss of motoneuron cell bodies and axonal degeneration. Although it is well known that loss of motoneurons at the lumbar spinal cord is an early event in the pathogenesis of the disease, it is not clear whether the corresponding proximal axons and NMJs are also early affected. In order to address this question, we have investigated the time course of the disease progression at the level of the motoneuron cell body, proximal axon (ventral root), distal axon (sciatic nerve), NMJ, and muscle fiber in *Nmd*^{2J} mice, a mouse model for SMARD1. Our results show an early and apparently parallel loss of motoneurons, proximal axons, and NMJs. In affected muscles, however, denervated fibers coexist with NMJs with normal morphology and unaltered neurotransmission. Furthermore, unaffected axons are able to sprout and reinnervate muscle fibers, suggesting selective vulnerability of neurons to Ighmbp2 deficiency. The preservation of the NMJ morphology and neurotransmission in the *Nmd*^{2J} mouse until motor axon loss takes place, differs from that observed in SMA mouse models in which NMJ impairment is an early and more general phenomenon in affected muscles.

Introduction

Spinal muscular atrophy with respiratory distress type 1 (SMARD1) is the second most common form of motoneuron disease in children, after proximal spinal muscular atrophy (SMA) (Bertini et al., 1989; Grohmann et al., 1999, 2001; Guenther et al., 2007). The disease normally manifests in the first two years after birth with a characteristic paralysis of the diaphragm and distal limb muscle atrophy. These pathological features correspond to motoneuron loss and muscle fiber degeneration, including myopathic changes which are prominent in the diaphragm (Diers et al., 2005; Grohmann et al., 2001; Rudnik-Schoneborn et al., 2004). As a monogenetic disorder, SMARD1 is caused by mutations in the *IGHMBP2* (Immunoglobulin μ-binding protein 2) gene on chromosome 11q13 which codes for an ATPase/Helicase that belongs to the SF1 superfamily (Grohmann et al., 2001; Guenther et al., 2009a; Jankowsky, 2011). However, little is known about the impact of the described cell specific abnormalities on the disease phenotype and its progression. In order to address this question we studied the neuromuscular degeneration mouse (*Nmd*^{2J}) as a model for the juvenile form of SMARD1. The *Nmd*^{2J} mouse carries a spontaneous point mutation in intron 4 of *Ighmbp2*, which leads majorly to an alternative spliced and truncated transcript (Cox et al., 1998). The mouse develops muscle weakness and atrophy, and also shows myopathic changes in the diaphragm at later disease stages (Cox et al., 1998; Grohmann et al., 2004). Former studies revealed that degeneration of muscle fibers in calf muscles appears relatively early in the second to third week after birth. In eight weeks old *Nmd*^{2J} mice, additional degenerative changes in the diaphragm were observed (Grohmann et al., 2004). However, motoneuron cell loss in *Nmd*^{2J} mice (~30%) is first detectable 10 days after birth, when these mice appear clinically healthy, accompanied by subtle axonopathic changes of the sciatic nerve. Loss of motoneurons remains within a constant level of about 30% until three weeks after birth, when *Nmd*^{2J} mice have developed hindlimb paralysis and a substantial number of degenerating axons in the sciatic nerve becomes detectable. At later disease stages motoneuron loss is mitigated (Grohmann et al., 2004). When Ighmbp2 expression is rescued selectively in neurons by transgenic methods, survival is prolonged but mice develop skeletal muscle degeneration and cardiomyopathy, indicating that disease pathology is complex and also directly affects striated muscles

* Corresponding author at: Institute for Clinical Neurobiology, Josef-Schneider-Str. 11, D-97080 Wuerzburg, Germany. Fax: +49 931 201 49788.
E-mail address: Jablonka_S@klinik.uni-wuerzburg.de (S. Jablonka).
Available online on ScienceDirect (www.sciencedirect.com).

0969-9961/$ – see front matter © 2013 Elsevier Inc. All rights reserved.
http://dx.doi.org/10.1016/j.nbd.2012.12.010

(Maddatu et al., 2004). Selective Ighmbp2 overexpression under a muscle-specific promoter erases the residing myopathy (Maddatu et al., 2005). Although these observations indicate cell autonomous disease mechanisms occurring both in muscles and nerves of the *Nmd^{2J}* mouse, the question which cellular components are mostly affected in skeletal muscle groups needs to be solved. Thus, we performed a morphometric and functional analysis of motor axons, NMJs, and skeletal muscle fibers focussing on the gastrocnemius, the diaphragm, and the levator auris longus muscle (LAL) from *Nmd^{2J}* mice.

Material and methods

Transgenic mouse lines

The *Nmd^{2J}* mouse line (Cox et al., 1998) was housed in the central animal facilities of the University of Wuerzburg and the University of Seville. It was kept on a C57Bl/6 background by backcrossing every 3 generations. The *thy1-YFP-H^{tg}* mice (YFP-12-H) originally described by (Feng et al., 2000) were obtained from Jackson Laboratories and also kept on a C57Bl/6 background in the animal facility in Wuerzburg. All described procedures and experiments were approved by the animal care and ethics committees of our institutions. In the *thy1-YFP-H^{tg}* mouse only few, but not all motoneurons are YFP positive. This has an important advantage that the axonal arborization of individual motoneurons can be investigated in target muscles in comparison to conventional staining with axonal markers like phospho-tau, which gives such a dense network of axonal processes that it is impossible to follow the branching of all axonal terminals from one individual motoneuron. The *thy1* promotor becomes active earliest 12 days after birth. Stable YFP expression is generally observed from P16 onwards. Therefore, we could detect both motoneuron cell bodies and axonal processes and their branching by *thy1*-YFP overexpression at symptomatic stages P16 and P21. Genotyping of *Nmd^{2J}* and the *YFP-H^{tg}* mouse line was performed as described previously (Cox et al., 1998; Feng et al., 2000).

Muscle and nerve histology

Preparation of the gastrocnemius muscle for immunohistochemistry

Mice were sacrificed by cervical dislocation, and the gastrocnemius muscle was dissected and immediately covered with 4% paraformaldehyde (PFA) and incubated for 20 min. After fixation single muscle fibers were teased. After washing with 0.1M Glycine in PBS for 30 min, the postsynaptic part of the neuromuscular junction was stained with α-Bungarotoxin Alexa Fluor 488 (1:500, Invitrogen) in PBS for 20 min. Subsequently, the muscle fibers were washed in PBS for 20 min and penetrated with ice-cold methanol for 2 min at −20 °C. After washing for 20 min with PBS a blocking solution containing 10% bovine serum albumin (BSA, Sigma) and 0.3% Triton X-100 was applied for 1 h. Rabbit polyclonal antibodies against neurofilament M (1:500, Millipore) and polyclonal guinea pig antibodies against Synaptophysin (1:500, Synaptic Systems) diluted in blocking solution were applied over night at 4 °C. Thereafter the muscle fibers were washed three times for 10 min in PBS. As secondary antibodies Cy3-conjugated polyclonal anti-guinea pig (1:400, Dianova) and Cy5-conjugated polyclonal anti-rabbit (1:400, Dianova) were diluted in the blocking solution and applied for 1 h at room temperature. Finally, the muscle fibers were washed three times in PBS for 10 min and mounted with a DABCO-Solution (9.97% PBS, 89.77% Glycerin and 0.26% DABCO, Merck) or Aqua PolyMount (Polysciences Inc.). For the morphological analysis of the neuromuscular endplate at P10, P16 and P21 three control and three *Nmd^{2J}* mice per time point were analyzed. The statistical difference between the genotypes was assessed using Student's unpaired two-tailed *t*-test (from GraphPad Prism Software). Results were considered statistically different when the p value was <0.05 and indicated by n.s. in case of non-significance. Exact p values, t values and degrees of freedom (df) are listed in the figure legend.

Whole mount preparation of the gastrocnemius muscle

The gastrocnemius muscles from adult *Nmd^{2J} thy1-YFP-H^{tg}* and *Nmd$^{+/+}$ thy1-YFP-H^{tg}* mice were squeezed between two object slides and fixed with 4% PFA for 30 min. After fixation of the muscle tissue, it was washed in PBS two times for 30 min. The postsynaptic part of NMJs was stained with α-Bungarotoxin Alexa Fluor 555 or 647 (1:500, Invitrogen) for 30 min. The muscle tissue was then washed in PBS for 2 h. Finally, the squeezed muscles were mounted with a DABCO-Solution (9.97% PBS, 89.77% Glycerin and 0.26% DABCO). Axon course and branching studies were performed with 8 control and 3 *Nmd^{2J}* mice for P16, and 9 control and 6 *Nmd^{2J}* mice for P21.

Quantification of muscle fiber size and dystrophin staining

Gastrocnemius and diaphragm muscles were prepared from mice immediately after cervical dislocation, embedded in OCT compound (Tissue Tek) and freshly frozen in nitrogen-cooled 2-methylbutane. Ten μm thick cryosections were prepared and stained with a standard HE protocol.

For the analysis of the fiber membrane and the NMJ innervation, gastrocnemius and diaphragm cross-sections were treated for 1 h with a blocking solution containing 10% BSA, 0.3% Triton X-100 in PBS. Muscle sections were then incubated overnight in blocking solution at 4 °C with a mouse monoclonal antibody against dystrophin (1:100, Novocastra), a rabbit polyclonal antibody against neurofilament M (1:500, Millipore) and bungarotoxin coupled to Alexa Fluor 555. Sections were then washed three times with PBS and incubated for 1 h at room temperature with a Cy2-conjugated anti-mouse (1:400, Dianova) and a Cy5-conjugated anti-rabbit (1:400, Dianova) secondary antibody. After three washing steps with PBS the sections were mounted with a DABCO-Solution (9.97% PBS, 89.77% Glycerin and 0.26% DABCO). The statistical significance of differences between control and *Nmd^{2J}* mice which is not depicted in Fig. 2, was assessed using the Student's unpaired two-tailed *t*-test (from GraphPad Prism Software): at P10 gastrocnemius muscle (12.9 ± 0.3 μm versus 13.1 ± 0.7 μm, $p = 0.7823$, $t = 0.2916$, $df = 5$ for 4 control and 3 *Nmd^{2J}* mice), at P21 gastrocnemius muscle (17.8 ± 0.3 μm versus 14.1 ± 1.0 μm, $^{*}p = 0.0131$, $t = 3.484$, $df = 6$ for 4 control and 4 *Nmd^{2J}* mice), at P42 gastrocnemius muscle (33.6 ± 1.0 μm versus 16.2 ± 0.7 μm, $^{***}p < 0.0001$, $t = 14.24$, $df = 6$ for 4 control and 4 *Nmd^{2J}* mice), at P10 diaphragm (13.5 ± 0.1 μm versus 13.8 ± 0.1 μm, $p = 0.1191$, $t = 1.978$, $df = 4$ for 3 control and 3 *Nmd^{2J}*), at P21 diaphragm (14.7 ± 0.1 μm versus 14.6 ± 0.2 μm, $p = 0.6743$, $t = 0.4526$, $df = 4$ for 3 control and 3 *Nmd^{2J}* mice), and at P42 diaphragm (18.6 ± 0.3 versus 14.0 ± 0.4, $^{***}p = 0.0006$, $t = 9.658$, $df = 4$ for 3 control and 3 *Nmd^{2J}* mice).

Preparation and staining of cryostat slices of sciatic nerves, spinal cord and ventral roots

Nmd^{2J} thy1-YFP-H^{tg} and *Nmd$^{+/+}$ thy1-YFP-H^{tg}* mice were perfused with 4% PFA and the sciatic nerves, ventral roots (L3–L6) and the lumbar part of the spinal cord were separated. After postfixation of the tissue with 4% PFA overnight, it had been transferred into a 30% sucrose solution. The tissues were then embedded in OCT compound and frozen within 2-methylbutane, cooled with liquid nitrogen. Subsequently, 10 μm thick cross-sections of sciatic nerves and ventral roots were performed; the spinal cords were cut in 15 μm thick cross-sections, respectively. For immunostaining, the sections were blocked with 10% BSA and 0.5% Triton X-100 in PBS for 1 h. Axons of the sciatic nerves and ventral roots were labeled overnight at 4 °C with a rabbit polyclonal antibody against neurofilament M (1:500, Millipore) whereas the motoneurons in the ventral horn of the spinal cord were stained with a goat polyclonal antibody against Choline Acetyltransferase (1:100, Millipore). Thereafter the slices were washed three times with PBS. The secondary antibodies Cy5

goat anti-rabbit and Cy5 donkey anti-goat were applied for 1 h at room temperature, respectively. Finally, the slices were washed three times with PBS for 10 min and mounted with a DABCO-Solution (9.97% PBS, 89.77% Glycerin and 0.26% DABCO). The quantitative analysis of spinal cord morphology included 4 control and 4 *Nmd*^{2J} mice at P16 and 3 control and 3 *Nmd*^{2J} mice at P21. For the quantification of YFP positive axons in the ventral roots we analyzed 4 animals per each genotype at P16 and 3 animals per genotype at P21. At P16, YFP positive motor axons in the sciatic nerve were counted in 4 control and 3 *Nmd*^{2J} mice, and at P21 three animals per genotype were studied. The statistical significance of differences between the genotypes was assessed by Student's unpaired two-tailed *t*-test using the GraphPad Prism Software. Results were considered statistically different when the p value was <0.05. Exact p values, t values and degrees of freedom (df) are indicated in the figure legends.

Imaging and confocal analysis

Imaging was acquired with an Olympus FluoView™ FV1000 confocal microscope. The final processing of all images was performed with MacBiophotonics ImageJ, Photoshop 7.0 (Adobe) and Illustrator CS5 (Adobe). Linear contrast enhancement was applied to images and all individual panels contained in these figures (Figs. 1A–C, 2D–I, 3A, B, 4A–I) were treated similarly.

Electromicroscopic studies of gastrocnemius muscle

Gastrocnemius muscles from 4 control and 3 *Nmd*^{2J} P21 mice were dissected as described above, and small tissue pieces were immediately fixed in 2% glutaraldehyde (GA) /2% PFA in PBS (12 h at 4 °C). After fixation, the muscle tissue pieces were thoroughly washed in PBS, postfixed in 1% OsO_4 for 1 h, and embedded in Epon (Serva, Heidelberg) following dehydration in ascending concentrations of ethanol including en-bloc contrasting using 2% uranylacetate (Serva, Heidelberg) in 70% ethanol for 1 h. Ultrathin sections of ~80 nm were cut on a Reichert-Jung ultramicrotome (Leica, Bensheim, Germany), mounted on formvar-coated nickel grids, contrasted with uranyl acetate and lead citrate (Reynolds, 1963), and observed using a Leo 912 AB transmission electron microscope (Carl Zeiss NTS, Oberkochen, Germany). The images shown in Fig. 5 were taken from one wildtype and one *Nmd*^{2J} mouse.

Histological and morphometric analysis of levator auris longus muscles

The levator auris longus (LAL) muscles from *Nmd*^{2J} and *Nmd*$^{+/+}$ mice were quickly dissected after killing the animals by CO_2 inhalation. Muscles were embedded in OCT compound, frozen in 2-methylbutane pre-cooled in liquid nitrogen, and stored at −80 °C until histological analysis. Histology was performed on muscle cryosections (10-μm thickness). Samples were collected on glass slides and were stained with hematoxylin/eosin (HE) or with the following primary antibodies for immunohistochemistry on unfixed transversal sections: mouse monoclonal anti-dystrophin antibody (clone MANDYS8, 1:400, Sigma); mouse monoclonal anti-eMHC (clone F1.652, undiluted supernatant, Developmental Studies Hybridoma Bank). Secondary antibodies were, respectively, goat anti-mouse IgG Alexa Fluor 488 (1:400, Invitrogen) and biotinylated anti-mouse antibody from the commercially available M.O.M. fluorescein kit (Vector laboratories). Immunostaining was performed according to manufacturer instructions. Stainings of the nuclei were performed with TO-PRO-3 from Sigma.

Neuromuscular junctions were labeled by incubation of the cryosections for 30 min at room temperature with α-bungarotoxin Alexa Fluor 488 conjugated (1:1500, Invitrogen) followed by sequential steps of PBS washing, 2% PFA fixation for 5 min, PBS washing, blocking with 5% horse serum and 0.1% Triton X-100 in PBS for 30 min and incubation over night with mouse monoclonal anti-Neurofilament H (SMI32, 1:1500, Covance). Primary antibody was revealed by incubation of the samples with Alexa Fluor 568- goat anti-mouse IgG (1:400, Invitrogen) for 2 h at 4 °C. Control experiments without primary antibody demonstrated that the signals observed were specific.

Digital images were acquired with a microscope DMR6000B (Leica) equipped with a DFC300FX camera for bright field color pictures and a Hamamatsu ORCA-ER camera for immunofluorescence. Morphometrical analyses were performed on digital pictures of muscle fibers that were outlined manually and their cross-sectional area was determined with the public domain computer-assisted image analysis software ImageJ (NIH, USA). GraphPad Prism software was used for statistical analyses of group comparisons and frequency distribution. The effect of the mutation on LAL myofiber size was assessed using the Wilcoxon–Mann–Whitney two-sample rank-sum test. A two-tailed analysis on 2160 myofibers from 6 different muscles (three mice per genotype) was performed and significance of differences was accepted at $p<0.05$.

Electrophysiological studies of LAL muscle

Muscle preparation

Mice were anesthesized with tribromoethanol (2%, 0.15 ml/10 g body weight, i.p.) and sacrificed by exsanguination. The LAL muscles were dissected with their nerve branches intact and pinned to the bottom of a 2 ml chamber, over a bed of cured silicone rubber (Sylgard, Dow Corning). Preparations were continuously superfused with a solution of the following composition (in mM): 125 NaCl, 5 KCl, 2 $CaCl_2$, 1 $MgCl_2$, 25 $NaHCO_3$ and 15 glucose. The solution was continuously gassed with 95% O_2 and 5% CO_2, which maintained the pH at 7.35. Recording was performed at room temperature (22–23 °C).

Intracellular recording

The nerve was stimulated by means of a suction electrode. The stimulation consisted of square-wave pulses of 0.2–0.5 ms duration and 2–40 V amplitude at variable frequencies (0.5–100 Hz). A glass microelectrode (10–20 MΩ) filled with 3M KCl was connected to an intracellular recording amplifier (Neuro Data IR283; Cygnus Technology) and used to impale single muscle fibers near the motor nerve endings. Evoked endplate potentials (EPPs) and miniature EPPs (mEPPs) were recorded from different NMJs within the muscle as described previously (Ruiz et al., 2008). Muscular contraction was prevented by including 3–4 μM μ-conotoxin GIIIB (Alomone Laboratories) in the bath, a specific blocker of muscular voltage gated sodium channels.

Data analysis

The mean amplitudes of the EPPs and mEPPs recorded at each NMJ were linearly normalized to −70 mV resting membrane potential. EPP amplitudes were corrected for nonlinear summation (McLachlan and Martin, 1981). Quantal content (QC) was estimated by the direct method, which consists of recording mEPPs and EPPs (nerve stimulation 0.5 Hz) simultaneously and then calculating the ratio: QC = Average Peak EPP/Average Peak mEPP. To evaluate the readily releasable pool (RRP) size the QC values during 1 s train of stimuli at 100 Hz were plotted against the cumulative number of quanta. The linear portion of the curve was back extrapolated. The x-intercept gives an estimate of RRP based upon the assumption of negligible mobilization of vesicles into the RRP (Elmqvist and Quastel, 1965) during the first 10–12 stimuli (Ruiz et al., 2011). All electrophysiological data are given as group mean values ± SEM, with n being the number of muscles fibers per group. A total of 33 myofibers from 7 muscles (3 control and 3/4 *Nmd*^{2J} mice) were analyzed. Measurements from different muscle fibers were grouped by mouse genotype. Statistical comparisons between *Nmd*^{2J} and control measures were made using Student's unpaired two-tailed *t*-test. Results were considered statistically different when the p value was <0.05. Additionally, we also analyzed the data with ANOVA including the mouse as a covariate for the data in order to detect whether particularly influential mouse's fibers drove the effect. No significant differences were found among groups, indicating that the influence of the individual mouse of a covariate was not significant in these series of experiments.

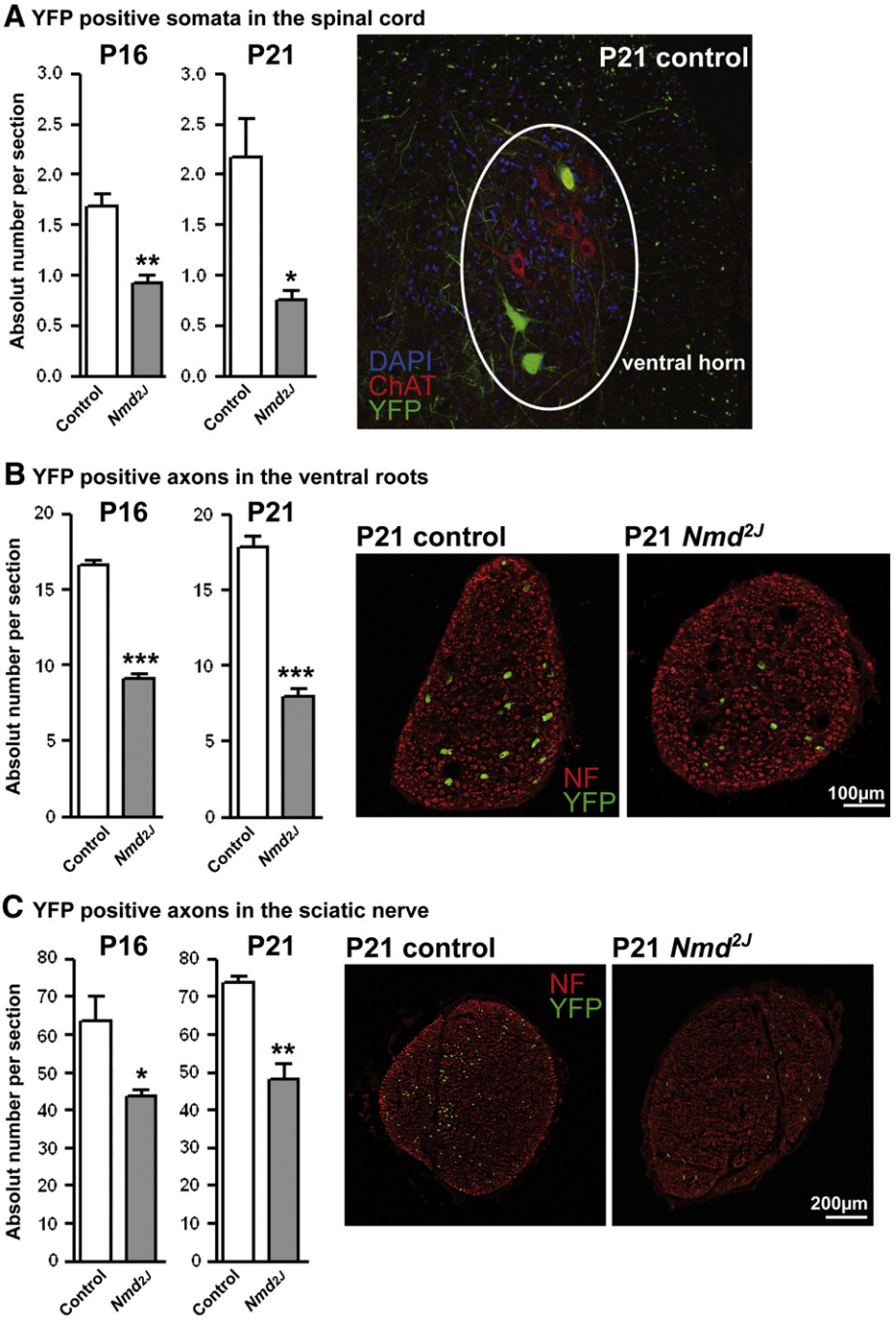

Fig. 1. Time course of motoneuron and motor axon loss in spinal cord, ventral roots, and sciatic nerve in *Nmd*^{2J} mice. (A) Number of YFP positive motoneurons is significantly reduced in P16 and P21 old *Nmd*^{2J} mice (at P16 1.7 ± 0.1 versus 0.9 ± 0.1, $^{**}p = 0.0021$, t = 5,159, df = 6 for 4 control and 4 *Nmd*^{2J} mice; and at P21 2.2 ± 0.4 versus 0.8 ± 0.1, $^{*}p = 0.0224$, t = 3.618, df = 4 for 3 control and 3 *Nmd*^{2J} mice). The reduction of the motor axon number keeps a comparable level over the ventral roots (at P16 16.6 ± 0.4 versus 9.1 ± 0.3, $^{***}p < 0.0001$, t = 16, df = 6 for 4 control and 4 *Nmd*^{2J} mice; and at P21 17.9 ± 0.7 versus 8.0 ± 0.5, $^{***}p = 0.0004$, t = 11,21, df = 4 for 3 control and 3 *Nmd*^{2J} mice) (B) up to the sciatic nerve (at P16 63.8 ± 6.5 versus 43.6 ± 2.0, $^{*}p = 0.0499$, t = 2.572, df = 5 for 4 control and 3 *Nmd*^{2J} mice and at P21 73.7 ± 1.7 versus 48.3 ± 3.8, $^{**}p = 0.0038$, t = 6.015, df = 4 for 3 control and 3 *Nmd*^{2J} mice) in (C). In all three neuronal compartments in *Nmd*^{2J} mice the relative reduction of motor fibers is constant. Representative pictures are shown for P21. Statistical analysis was performed using Student's unpaired two-tailed *t*-test. Bars represent mean ± SEM, significance is indicated by stars ($^{*}p < 0.05$; $^{**}p < 0.01$; $^{***}p < 0.001$).

Results

Early loss of motoneurons in lumbar spinal cord and proximal motor axons in L3-6 ventral roots in Nmd^{2J} *mutants*

Here, in order to study further the development of the pathophysiological cascade leading to muscular atrophy in *Nmd*^{2J} mice, we investigated the temporal relationship between motoneuron cell body loss in the spinal cord and the corresponding motor axon loss in the ventral roots. In addition, we quantified axon loss in the sciatic nerve. For this purpose, we used *thy1-YFP-H*^{tg} *Nmd*^{2J} mice which allow easy tracking of motor axons and their terminal branches along the spinal cord-muscle axis. *Thy1*-YFP expression in motoneurons starts at P12 (Caroni, 1997), with robust expression from P16 onwards. Less than

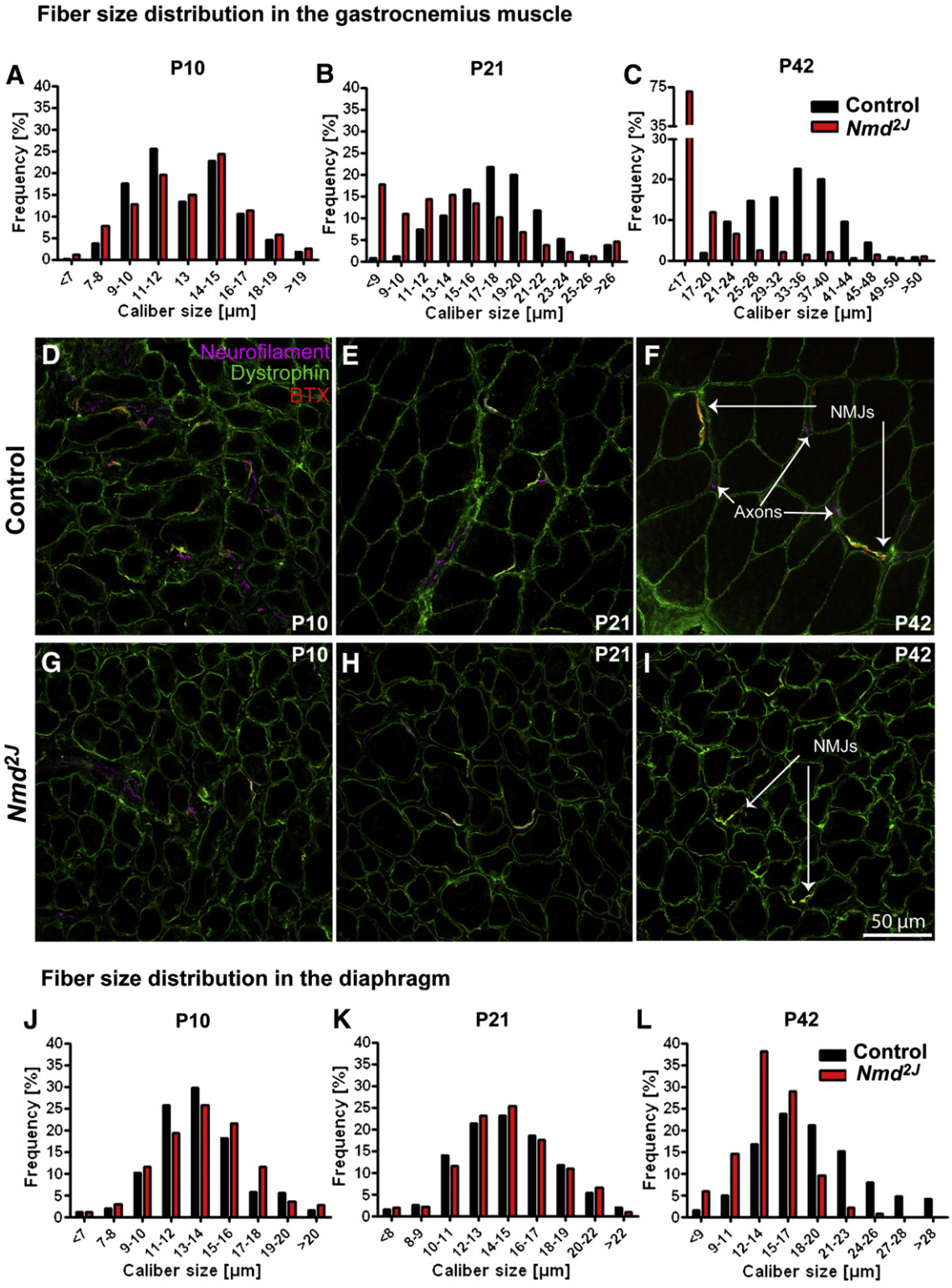

Fig. 2. Time course of fiber atrophy in gastrocnemius and diaphragm muscle from *Nmd*^{2J} mice. (A–C) Fiber caliber size distribution in the gastrocnemius muscle at three different time points (P10, P21, P42) in *Nmd*^{2J} and control mice. Neurofilament (magenta), dystrophin (green) and BTX (red) stainings are depicted in (D–F) for control mice and in (G–I) for *Nmd*^{2J} mice. The fiber caliber size distribution of the diaphragm from *Nmd*^{2J} and control mice at P10, P21 and P42 is shown in (J–L). The mean caliber size of control fibers is determined. First value of each graph is 50% less than the mean value of the control fibers. The final value is higher than 150% of the mean value of the control fibers. The values of the statistical differences are indicated in the material and method part.

10% of all motor axons of the *thy1-YFP-H*^{tg} mouse line are labeled (Feng et al., 2000), allowing reliable analysis of the arborisation of axonal processes from individual motoneurons. The number of labeled axons observed was consistent with the quantitative analysis of YFP positive motoneuron cell bodies in the spinal cord of the examined control mice (P16 and P21). On average, 1–2 cell bodies per 15 µm cryosection express YFP, thus the obtained data are not comparable to the data from (Grohmann et al., 2004), where the absolute number of spinal

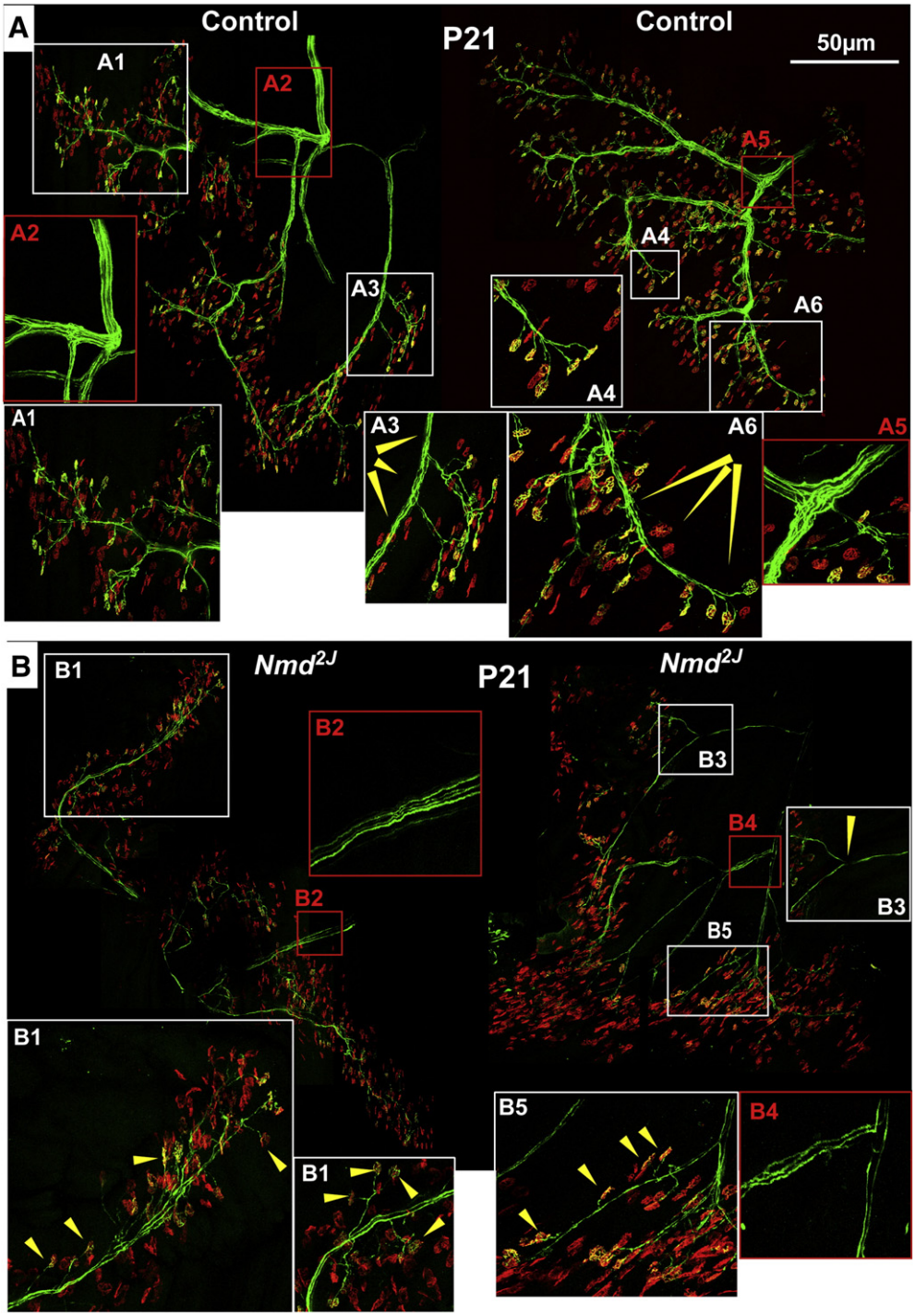

Fig. 3. Axon arborization and sprouting at P16 and P21 in *Nmd*^{2J} gastrocnemius muscle. (A, B) YFP positive motor axons from controls at P21 show similar axon course (A) but thicker axon bundles in the medial part at the muscle entry in contrast to *Nmd*^{2J} (B). In *Nmd*^{2J} mice the number of YFP positive motor axons is declined (A2 and A5, B2 and B4; insets) and the arborization is less (A1, A6, B1, B5), but the percentage of the frequency of small additional sprouts (A1, A3, A4, A6, B1, B3, B5, yellow arrow heads) is increased (Table 1). For P21, 9 control and 6 *Nmd*^{2J} mice were analyzed; and for P16, muscles from 8 control and 3 *Nmd*^{2J} mice were taken.

motoneurons was determined. We included cryosections from L3 to L6 of the spinal cord into our counts and compared the absolute number of YFP positive cell bodies from control and *Nmd*^{2J} mice at P16 and P21. At both time points, YFP positive spinal motoneuron cell bodies are significantly reduced in *Nmd*^{2J} mice (Fig. 1A; at P16, the reduction was 1.7 ± 0.1 in control versus 0.9 ± 0.1 in *Nmd*^{2J} mice, and at P21 2.2 ± 0.4 in control versus 0.8 ± 0.1 in *Nmd*^{2J} mice, with a representative image for controls). We subsequently determined the number of YFP positive axons in the ventral roots in control and *Nmd*^{2J} mice and found a reduction of YFP positive motor axons that parallels the loss of motoneurons (at P16 16.6 ± 0.4 versus 9.1 ± 0.3 and at P21 17.9 ± 0.7 versus 8.0 ± 0.5) (Fig. 1B with representative images). We then investigated axons within the sciatic nerve. The sciatic nerve contains sensory and motor fibers which hardly can be discriminated. Quantitative analysis shows a

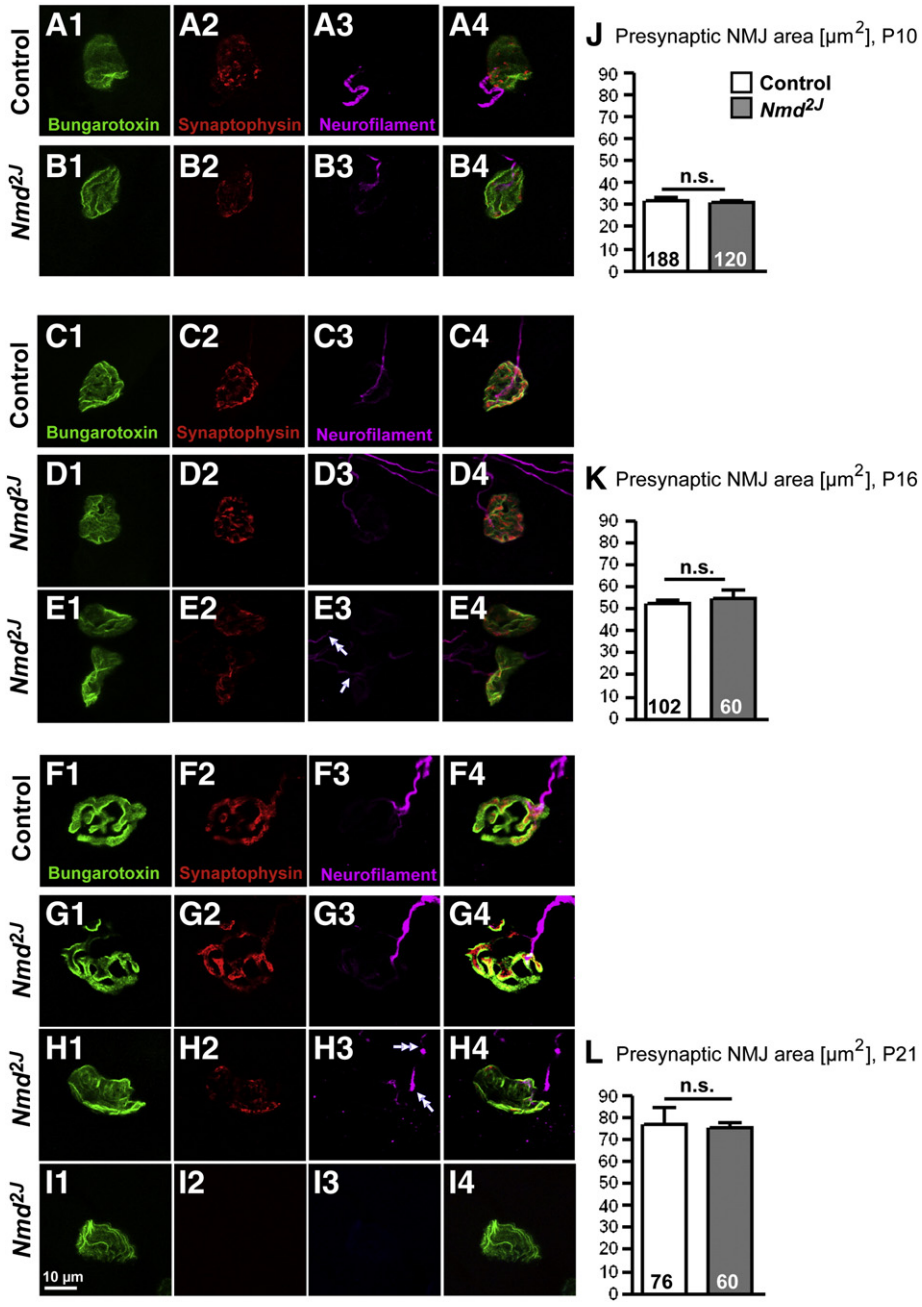

Fig. 4. Coexistence of intact and denervated neuromuscular endplates in the gastrocnemius muscle from *Nmd*^{2J} mice between P10 and P21. α-Bungarotoxin, synaptophysin and neurofilament are similar distributed in P10 control (A1–A4) and *Nmd*^{2J} motor endplates (B1–B4). The bar diagram in (J) depicts no markedly size difference of intact presynapses between *Nmd*^{2J} and control NMJs (31.9 ± 1.1 µm versus 30.7 ± 1.3 µm, p = 0.5188, t = 0.7065, df = 4 for 3 control and 3 *Nmd*^{2J} mice). (C1–D4) shows that Bungarotoxin, synaptophysin and neurofilament are equally distributed in control NMJs and intact *Nmd*^{2J} NMJs at P16. The presynaptic NMJ size of *Nmd*^{2J} muscles is similar to that analyzed from controls (52.4 ± 1.5 µm versus 54.9 ± 3.6 µm, p = 0.5559, t = 0.6418, df = 4 for 3 control and 3 *Nmd*^{2J} mice) (K). Only some of NMJs exhibit "degenerative signs" such as degenerating axons (E3, double arrow) and dotted synaptophysin distribution (E2) in contrast to intact axon innervating the NMJ (E3, arrow). (F1–F4) displays the intracellular distribution in P21 NMJs of acetylcholine receptors (BTX in green) postsynaptically and neurofilament (magenta) as well as the presence of synaptophysin (red) presynaptically. (G1–I4) depicts the α-Bungarotoxin (green), the neurofilament (magenta) and the synaptophysin (red) localization in *Nmd*^{2J} NMJs. Nearly half of all analyzed junctions in *Nmd*^{2J} mice at P21 show a pretzel-like structure (G1–G4) and a similar distribution of acetylcholine receptors (BTX in green), neurofilament (magenta) and synaptophysin (red). (H1–H4) Some NMJs at P21 in *Nmd*^{2J} exhibit a denervating process: NMJs lose their pretzel-like structure (H1, H4), the synaptophysin stain becomes weaker (H2, H4) and axons start to degenerate (double arrows in H3). Nearly half of all examined junctions in *Nmd*^{2J} mice at P21 are denervated (I1–I4). Neurofilament as well as synaptophysin stainings are completely abolished (I2–4). The quantification of the NMJ presynapse size of *Nmd*^{2J} and control endplates in (L) discloses no reduction (76.6 ± 8.0 µm versus 75.1 ± 2.7 µm, p = 0.8681, t = 0.1770, df = 4 for 3 control and 3 *Nmd*^{2J} mice). The residual α-Bungarotoxin staining (green) (I1, I4) at the postsynapse, shows a clear plaque-like structure. The single values were obtained from at least 60 endplates of 3 different mice per genotype and postnatal stage. The number of NMJs analyzed per phenotype is indicated in each bar. Statistical analysis was performed using Student's unpaired two-tailed *t*-test. Bars represent mean ± SEM, non-significance is indicated by n.s.

significant reduction of YFP positive axons both at P16 (63.8 ± 6.5 versus 43.6 ± 2.0) and P21 (73.7 ± 1.7 versus 48.3 ± 3.8) (Fig. 1C with representative images).

These findings indicate that motoneuron cell body loss corresponds to motor axon loss along the whole spinal cord-motor nerve axis even at early disease stages (P16 and P21).

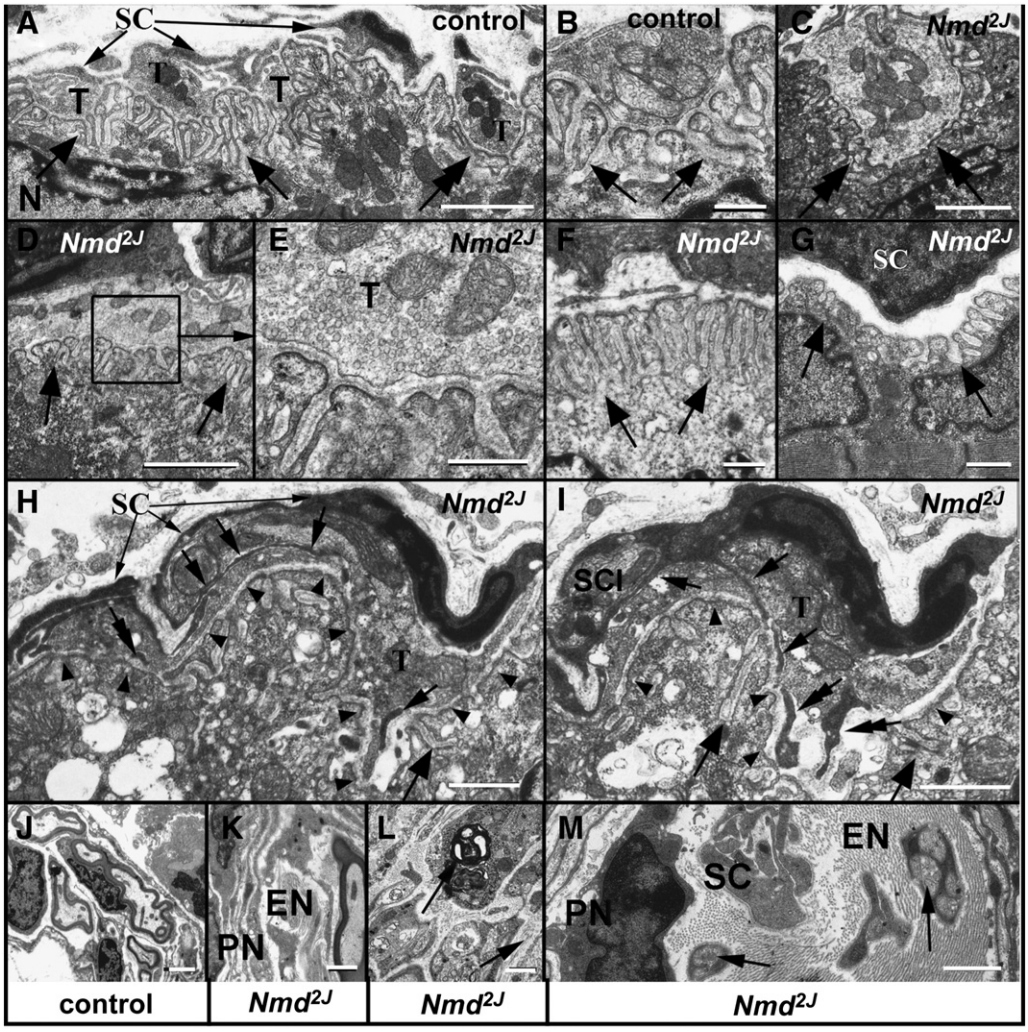

Fig. 5. Ultrastructural alterations in the gastrocnemius muscle of NMJs from P21 *Nmd^{2J}* mouse and controls. (A, B) NMJs in control mice show vesicle- and mitochondria-filled terminals (T) opposed to postsynaptic membrane areas displaying well-developed (large arrows in A, B) and, less frequently, irregular and/or shallow junctional folds (double arrow in A) and terminal Schwann cells (SC) covering the terminals with intertwined thin processes (small arrows in A). (C–I; box in D shown at higher magnification in E; H, I: serial sections) Some NMJs in P21 *Nmd^{2J}* mice show comparatively normal morphology (C–E) with somewhat less elaborate junctional folds than observed in the controls (double arrows in C, arrows in D). Frequently, postsynaptic areas without associated terminals and junctional folds displaying differential degrees of elaboration are observed (arrows in F, G). Occasionally, NMJs with signs of pre- and postsynaptic degeneration are found (H, I: serial sections of one NMJ) with subsynaptic membrane (arrowheads) showing only individual normal junctional folds (large arrows) and vacuolized subsynaptic sarcoplasm, and Schwann cells extending narrow processes (small arrows) into the widened synaptic cleft (double arrows) and completely enveloping a terminal (T) or parts of the pre-terminal axon (Schwann cell inclusion, SCI; I). Intramuscular nerve fascicles in *Nmd^{2J}* mice (K, L, M), which in control (J) mice contain numerous well-myelinated large-caliber axons, show individual normal appearing myelinated axons (K) in addition to signs of degeneration with Schwann cells containing myelin debris (arrow in L) or devoid of axons and myelin resembling Büngner bands (SC/arrow in M, SC) and abundant endoneurial collagen (EN; K, M). Gastrocnemius muscles from 4 control and 3 *Nmd^{2J}* mice were analyzed, images A, B and C–I are from specimen of one control and one *Nmd^{2J}*mouse, respectively. Bars in A, C, D, H, and I: 2 μm, in B, E, and G: 500 nm, PN: perineurium. Bars in: K, L, M: 1 μm, in E: 5 μm, in J, F: 2 μm.

Atrophy in the gastrocnemius muscle occurs at P21 in Nmd^{2J} mutant mice and correlates with the development of hindlimb paralysis

In order to explore the correlation between motor neuron/axon loss and muscle fiber degeneration, we measured the caliber size of gastrocnemius muscle fibers at three different time points of disease progression. At P10, when *Nmd^{2J}* mice are still clinically asymptomatic, at P21, when all the *Nmd^{2J}* mice show clear disease features and motor axon loss is already prominent (see Fig. 1), and at P42, a late disease stage. The morphological studies were done mainly with the gastrocnemius muscle, since we know from previous experiments, that this muscle is made up of mostly fast-twitch muscle fibers and it is highly affected. Thus subtle morphological alterations during disease progression are well quantifiable. We also compared the data with those obtained from the diaphragm which is not affected by motor axon loss in the phrenic nerve (unpublished data and Grohmann et al., 2004). We measured the distribution of caliber sizes of muscle fibers (Fig. 2). At P10, neither the diaphragm nor the gastrocnemius muscle showed any fiber caliber size reduction (Figs. 2A, D, G, J). At P21, when the *Nmd^{2J}* mice are phenotypically affected, the fiber caliber size of the skeletal muscle shows a shift to smaller fibers (Figs. 2B, E, H) and a significantly reduced mean value (17.8 ± 0.3 μm in control versus 14.1 ± 1.0 μm in *Nmd^{2J}* mice, see also material and method part), whereas the diaphragmatic fibers are still unaffected at P21 (Fig. 2K). At a later disease stage (P42), both muscle types exhibit a clear and highly significant fiber size reduction with a shift to smaller fibers (Figs. 2C, F, I, L). Staining with antibodies against dystrophin revealed that muscle fiber membranes of *Nmd^{2J}* mutant fibers in the gastrocnemius muscle are intact at all time points (Figs. 2G–I) similar to the control situation (Figs. 2D–F). The same result was obtained for muscle fibers in the diaphragm (data not shown). Muscle fibers also exhibit intact postsynaptic structures, as revealed by BTX stainings which in many cases correlates with motor fiber presynaptic innervation, as

shown by Neurofilament staining. At later disease stages, denervated postsynapses (arrows in Fig. 2I) could be monitored (see also below).

Altered motor axon terminal arborization in the gastrocnemius muscle of Nmd^{2J} mice

To follow the YFP-positive motor axons to their terminals at the gastrocnemius muscle, we investigated axonal telodendron elaboration between P16 and P21, the time points at which loss of YFP positive motoneuron cell bodies and proximal axons is ~50% (see Figs. 1A, B). We studied the medial part of the gastrocnemius muscle at P16 and P21. Images from P21 are depicted in Fig. 3, quantification data from P16 and P21 are shown in Table 1. The presynaptic compartments and axon bundles from representative mice at P21 are shown in Fig. 3A (control), and in Fig. 3B (*Nmd^{2J}*). The motor axon course in *Nmd^{2J}* mutant muscles was not altered at P16 or P21, but the number of YFP positive axons seemed to be reduced (Figs. 3B2, B4) in comparison to controls (Figs. 3A2, A5). However, quantification of terminal arborization/sprouting in both genotypes (Figs. 3A3, A6 for controls and B1, B3, B5 for *Nmd^{2J}* mice, indicated by yellow arrow heads) revealed an increasing number of YFP positive axons which end up in more than 3 NMJs in the mutant situation between P16 and P21 (Table 1). This finding is in agreement with the report by Ruiz et al., who monitored a significant enlargement of motor units in *Nmd^{2J}* mice (Ruiz et al., 2005), and indicates that compensatory mechanisms occur in *Nmd^{2J}* mice, similar as in mouse models of mild forms of spinal muscular atrophy such as SMA type III models (Simon et al., 2010).

Denervated and intact motor endplates between P10 and P21 in Nmd^{2J} mice

The capability for sprouting requires an intact nerve ending. The presence of presynaptic terminals does not necessarily imply that the synapse functions normally. As a first step, we therefore started a morphological analysis of the NMJs of the gastrocnemius muscle from *Nmd^{2J}* and control mice at P10, before paralysis becomes apparent, and at P16 and P21, when first pathological signs have been manifested. The shape of the NMJs from control and *Nmd^{2J}* mice at P10, a stage where motoneuron cell loss in *Nmd^{2J}* mice is already detectable, was more plaque-like (Figs. 4A, B), while the shape in control NMJs and in intact NMJs from *Nmd^{2J}* mice at P16 and P21 was almost pretzel-like (Figs. 4C, D, F, G). We used confocal microscopy to investigate distribution of synaptic vesicles at the NMJs visualized by α-synaptophysin staining. In parallel, preterminal and terminal axon course was investigated by α-neurofilament staining, and the postsynaptic compartment by staining of acetylcholine receptors with α-Bungarotoxin. Quantification of presynaptic areas of innervated NMJs from P10 *Nmd^{2J}* mice and controls revealed no significant differences (Fig. 4J). The NMJ shape and the subcellular distribution of axonal neurofilament, presynaptic synaptophysin, and acetylcholine receptors at postsynaptic sites were also unchanged (Figs. 4A1-B4), confirmed by an unchanged transcript level of the acetylcholine receptor at P10 in *Nmd^{2J}* mice (data not shown). At P10, a time point when polysynaptic innervation is still detectable (Brook and Duchen, 1990), we quantified the relation of innervated, denervated and "degenerative" NMJs in *Nmd^{2J}* mutant muscles and found that 34% of the NMJs were denervated and 2% exhibit degenerative signs (Table 2). At day 16 after birth, NMJs in control mice showed an approximately pretzel-like shape (Figs. 4C1-C4); and at three weeks after birth, NMJs are normally fully developed and show a presynaptic and postsynaptic pretzel-like structure (Figs. 4F1-F4). The dotted synaptophysin distribution in the presynaptic compartment shown in Figs. 4C2, C4 and F2, F4 represents the vesicle localization relative to the postsynapse (Figs. 4C1, C4 and F1, F4). At both developmental stages (P16 and P21) about half of the NMJs in *Nmd^{2J}* mice presented normal structural traits (Table 2). First and surprisingly, numerous innervated NMJs were observed which display continuous axonal neurofilament staining and normal pretzel-like synaptophysin and acetylcholine receptor distribution, thus representing intact terminal axons, presynaptic terminals, and postsynapses (Figs. 4D1-D4 and G1-G4). The size of these intact presynapses did not vary between mutant and control NMJs at P16 and P21 (Figs. 4K and L); however some of the documented *Nmd^{2J}* mutant NMJs (3–4%) showed signs of ongoing axonal degeneration (Table 2), indicated by fragmented magenta neurofilament staining (Figs. 4E3 and H3, double arrows) and altered synaptophysin distribution (Figs. 4E2 and H2). Other NMJs completely lacked innervation and displayed a plaque-like morphology (Figs. 4I1-I4). Quantification of the relative number of NMJs in each subgroup between P16 and P21 in *Nmd^{2J}* mice showed that the percentage of intact endplates was between 50% and 55%, completely denervated NMJs between 42% and 46%, while the NMJs displaying "degenerative signs" represented a minority of 3–4% of all examined endplates (Table 2). The slight but statistically not significant increase in number of intact endplates (50% at P16 and 55% at P21 in Table 2) is probably due to increased sprouting (Table 1).

The results from this morphological analysis are summarized in Table 2. From P10 to P21 NMJs of *Nmd^{2J}* mice showed an increase of denervated NMJs (34% to 42%) and a decrease of intact NMJs (64% to 55%). NMJs with obvious "degenerative" signs such as a "dotted" synaptophysin staining and fragmented axons at the presynapse keep a constant level from 2–4% along the time course. These results indicate that the degenerative process at *Nmd^{2J}* mutant NMJs is hard to visualize, since only a minority of NMJs displays degenerative presynaptic features whereas the majority of the endplates is intact or completely denervated. In controls no NMJs with degenerative signs are detectable, only a minority of 3–6% which are not α-neurofilament positive are observed (data not shown).

We also performed ultrastructural analyses of the gastrocnemius muscle at P21 when muscle weakness is manifest. In control muscle, NMJs generally showed presynaptic terminals filled with vesicles and mitochondria, postsynaptic areas with deep basal lamina-lined junctional folds, and terminal Schwann cells (SC) extending numerous thin processes to cover the terminals (Figs. 5A, B). Junctional fold areas not associated with terminals or containing few and/or shallow folds indicative of synaptic rearrangement (Cardasis and Padykula, 1981) or immaturity (Noakes et al., 1995) were rare (Fig. 5A, double arrow). In *Nmd^{2J}* mutant gastrocnemius muscle, fiber degeneration was observed and few NMJs or NMJ remnants were encountered in ultrathin sections. In specimen derived from one *Nmd^{2J}* mouse, NMJs could be classified into roughly three morphological categories. Firstly, comparatively normal NMJs were found displaying vesicle-filled

Table 1
Quantification of axonal sprouting in control and *Nmd^{2J}* mice.

NMJs/axon	P 16		P21	
	Control	*Nmd^{2J}*	Control	*Nmd^{2J}*
1	49 (79%)	10 (56%)	246 (85%)	9 (13%)
2	11 (18%)	4 (22%)	42 (15%)	24 (35%)
3	2 (3%)	2 (11%)	0	16 (23%)
4	0	2 (11%)	0	7 (10%)
≥5	0	0	0	13 (19%)

Table 2
Quantification of NMJ morphology in control and *Nmd^{2J}* mice.

NMJ morphology	P10		P16		P21	
	Control	*Nmd^{2J}*	Control	*Nmd^{2J}*	Control	*Nmd^{2J}*
Intact	178 (97%)	82 (64%)	97 (94%)	60 (50%)	62 (95%)	33 (55%)
Denervated	6 (3%)	44 (34%)	6 (6%)	55 (46%)	3 (5%)	25 (42%)
Degenerating	0	3 (2%)	0	5 (4%)	0	2 (3%)

presynaptic terminals and postsynaptic junctional folds appearing less elaborate than in control NMJs (Figs. 5C-E). Secondly, junctional fold areas lacking associated terminals throughout serial sections were observed which occasionally contained deeply invaginated (Fig. 5F) but mostly shallow and disorganized folds (Fig. 5G). These apparently denervated NMJs constituted the majority of putative NMJs in all analyzed *Nmd^{2J}* mutant muscles. Thirdly, few NMJs were found which showed signs of presynaptic degeneration with terminals partially disattached from the subsynaptic membranes, signs of postsynaptic degeneration, and SCs extending narrow processes between the terminals and the junctional basal membranes, occasionally completely enveloping parts of preterminal axons (Figs. 5H, I). Intramuscular nerves in controls were filled with numerous well-myelinated axons (Fig. 5J). In *Nmd^{2J}* mutant muscle, some healthy-appearing myelinated axons were observed in addition to abundant endoneurial collagen, numerous non-myelinated nerve fibers, and SCs containing axon/myelin debris or lacking axons resembling Büngner bands (Figs. 5K-M).

The outcome of our ultrastructural studies confirms our data obtained from confocal microscopy. We found either intact or denervated NMJs. Degenerative signs in *Nmd^{2J}* mutant NMJs did not correspond to vesicle deprivation and neurofilament invasion, as observed in mouse models of SMA (Cifuentes-Diaz et al., 2002; Kong et al., 2009; Park et al., 2010; Ruiz et al., 2010; Torres-Benito et al., 2011). The prominent degenerative axonal phenotype in *Nmd^{2J}* mice postulates a disease mechanism which does not primarily affect the NMJs as observed for the SMA mice.

No alterations in spontaneous and evoked neurotransmitter release in motor endplates of affected LAL muscle from Nmd^{2J} mice at late disease stages

These structural data open the question whether the functionality of remaining NMJs in a given muscle was disturbed. We used the LAL muscle for the functional studies because it represents an affected fast-twitch muscle where the degenerative changes were still not prominent when we could start electrophysiological analyses. This allowed us to explore function before less specific changes resulting from massive neurodegeneration took place. Therefore it is more convenient for investigating the primary alterations in the motoneurons, without much interference from secondary changes due to muscular atrophy and terminal degeneration. We examined spontaneous and evoked neurotransmission by studying miniature endplate potentials (mEPPs) and evoked endplate potentials (EPPs) in the LAL muscle of two months old control and *Nmd^{2J}* littermates, at a time point when the mice were fully symptomatic.

First we checked whether LAL muscle fibers were morphologically affected by the disease. Comparison of Hematoxylin and eosin stainings from control and *Nmd^{2J}* mice showed clear signs of atrophic fibers in *Nmd^{2J}* mutant LAL muscles (Figs. 6A and B). Quantitative analysis of myofiber cross-sectional area (Fig. 6C) confirmed a severe size reduction in *Nmd^{2J}* mutant muscle fibers. For further confirmation of muscle pathology, we investigated the distribution of nuclei within the fibers (Figs. 6D, E) and the presence of fibers expressing the embryonic myosin heavy chain (eMHC) isoform (Figs. 6F, G). *Nmd^{2J}* mutant muscles were characterized by the presence of fibers with central nuclei (white arrow heads in E) and the presence of eMHC (white arrow heads in G). Embryonic MHC is normally absent in adult myofibers but it is re-expressed after denervation or paralysis (Schiaffino et al., 1988). The observed morphological alterations refer directly to an ongoing LAL muscle degeneration in *Nmd^{2J}* mice. Second, we investigated the degree of muscle fiber denervation. We found some denervated NMJs (Fig. 6I, arrow head), but many muscle fibers still showed intact NMJs (Fig. 6K, arrow heads) in *Nmd^{2J}* mice. Intact NMJs from control mice are shown in Figs. 6H and J (arrow head). As we figured out that the LAL muscle in affected *Nmd^{2J}* mice show degenerative signs without highly affected NMJs, we started the electrophysiological analyses of neurotransmission.

We first compared the characteristics of mEPPs and found that the amplitude and frequency of mEPPs were not statistically different between control and *Nmd^{2J}* mice (Figs. 6L, M). We next compared the size and shape of evoked endplate potentials. Neither the EPP amplitude (Figs. 6N, O) nor the mean quantum content, which represents the number of vesicles, that release neurotransmitter in response to a single action potential (Fig. 6P) was statistically different between control and mutant terminals. Neither the mean EPP rise time, measured between 10 and 90% on the leading edge of the peak, nor the decay phase of EPPs, measured from the 50% of the peak amplitude to the baseline, was significantly different in *Nmd^{2J}* and in control mice (Fig. 6Q).

Finally, we investigated whether the size of readily releasable pool (RRP) of synaptic vesicles in control and *Nmd^{2J}* mice were different. To estimate the size of the RRP, quantum content (y axis) was plotted against accumulated quantum content (Fig. 6R), and a straight line was drawn through the declining phase as described in Ruiz et al., 2011; its x-axis intercept gives an estimate of the RRP size. In control and *Nmd^{2J}* mice the mean size of the RRP was not different (Fig. 6S).

Repetitive nerve stimulation and nerve-muscle coupling

Electrophysiological recordings from synaptic terminals in the LAL muscle in two-months old *Nmd^{2J}* mice showed that during nerve repetitive stimulation trains a fraction of the stimuli failed to evoke postsynaptic responses, producing the so called failures (Fig. 7A, right traces). No failures were observed in control terminals, as expected (Fig. 7A, left traces). Interestingly, in mutant terminals, the amplitude of EPPs during the periods of non-failure was not significantly different from that in control terminals under repetitive stimulation (data not shown). This finding suggests that the failures were not due to a sudden defect in synaptic vesicle availability, calcium entry, or in the release machinery, as in those cases variability in the size of the responses is expected instead of all-or-none signals. To confirm this point we calculated the theoretical probability of failures (P_f), which is inversely correlated with the number of released vesicles per action potential (quantal content, QC). That is, the lower the QC the most probably is that no vesicle, or a low number of vesicles, fuse with the plasma membrane in response to a stimulus. Control and mutant terminals have a QC of ~30 (Fig. 6P), so P_f, calculated as $P_f = e^{-QC}$ (Ruiz et al., 2005), was ~10^{-13}. Even assuming a 50% decrease of QC during the plateau phase of the train (Ruiz et al., 2011), the theoretical P_f was very low (<10^{-6}). However, the actual P_f, calculated from the recordings, at different stimulation frequencies, was much higher than predicted in *Nmd^{2J}* mice, and directly related with the stimulation frequency (Fig. 7B). These results suggest that the failures were caused upstream of neurotransmitter release, most probably by a defect in axonal conduction of action potential.

The electrophysiological data imply that NMJs in *Nmd^{2J}* mutant muscles preserve their functionality to the time point when axonal degeneration occurs. The axonal degenerative process therefore is independent from neurotransmitter release impairments.

Discussion

In this study, we found that loss of lumbar spinal motoneurons and corresponding proximal and distal axons occurs early, just when first signs of atrophy of the gastrocnemius muscle are observed in *Nmd^{2J}* mice (at P16 and continued up to P21). Neurotransmission, as measured by electrophysiological techniques at individual motor endplates in the LAL muscle appears normal as long as the NMJs are innervated. *Nmd^{2J}* mice differ from mouse models of severe SMA (Monani et al., 2000) or intermediate forms of SMA in which motoneuron loss is only observed when paralysis is clearly detectable (Michaud et al., 2010; Monani et al., 2000, 2003). In contrast to *Nmd^{2J}* mice, alterations of neurotransmission are prominent in mouse models for intermediate

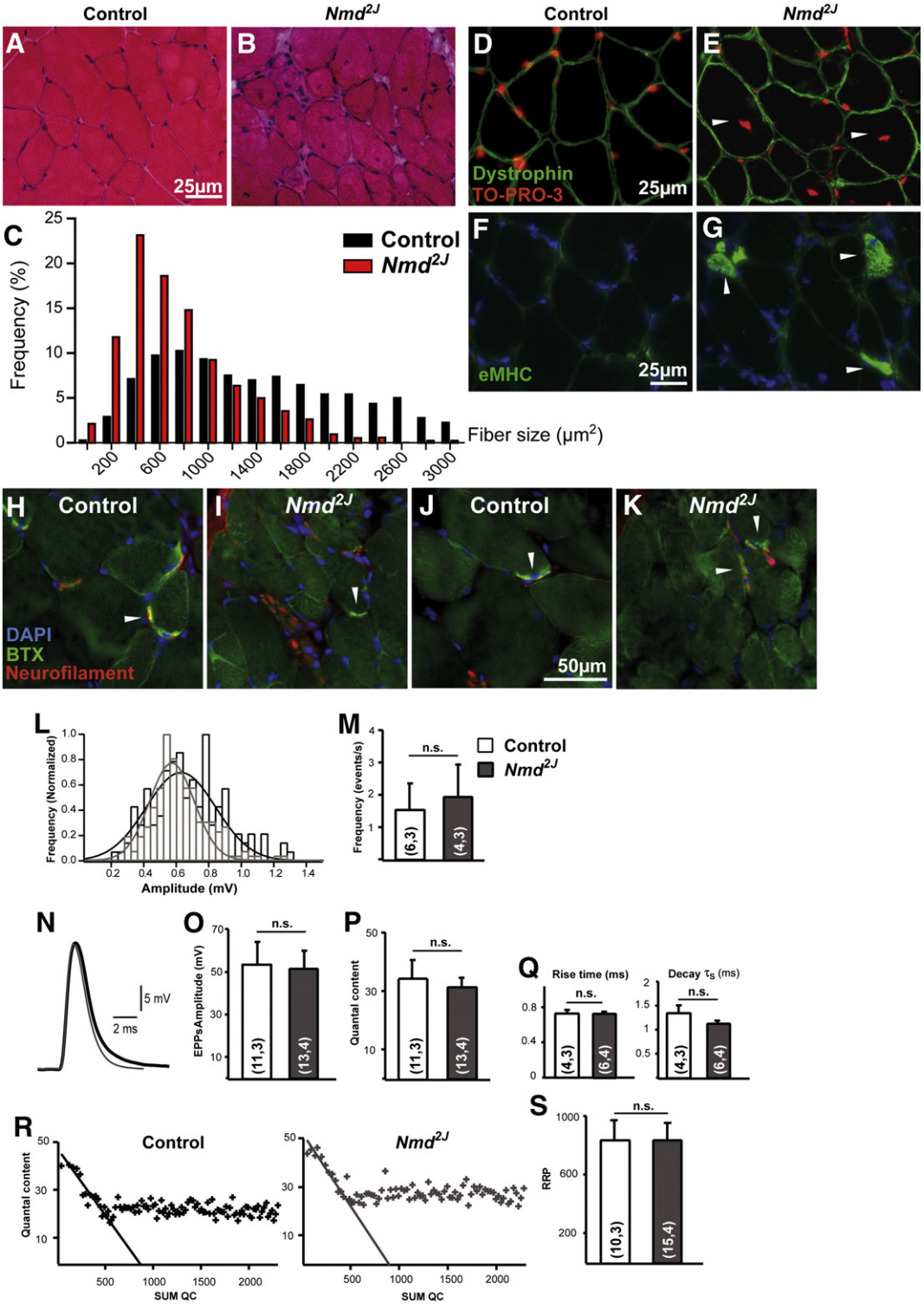

Fig. 6. No alteration in spontaneous and evoked neurotransmitter release in the LAL muscle of *Nmd^{2J}* mice. (A, B) Representative pictures of Hematoxylin and Eosin staining of LAL muscle from two months old control (A) and age-matched *Nmd^{2J}* mice (B). (C) Fiber size distribution reveals reduced fiber size in *Nmd^{2J}* mutant muscle (1559 ± 34 µm^2 versus 762 ± 14 µm^2, Wilcoxon–Mann–Whitney U = 237700, two-tailed $p<0.0001$, df = 1 on 2160 myofibers analyzed from 6 different muscles of 3 control and 3 *Nmd^{2J}* mice). (D, E) Abnormal nuclei localization in *Nmd^{2J}* fibers is indicated by a TO-PRO-3 staining. (F, G) Presence of fibers expressing embryonic myosin heavy chain (eMHC) in affected LAL muscle. Localization of NMJs in LAL muscles from control (H, J) and *Nmd^{2J}* mice (I, K). (L, M) Control versus Nmd^{2J} mEPP amplitude (L) (1.7 ± 0.2 mV versus 1.7 ± 0.2 mV, $p = 0.83$, $t = 2.07$, $df = 22$) and frequency (M) (1.6 ± 0.8 events/s versus 2.0 ± 0.9 events/s, $p = 0.74$, $t = 2.3$, $df = 8$) distributions were not statistically different for 3 control and 3 *Nmd^{2J}* mice. (N) Representative recordings of evoked endplate potentials (EPPs) in control (gross trace) and *Nmd^{2J}* mutant LAL muscles (light trace). Mean EPP amplitudes (O) (54.4 ± 10.2 mV versus 51.4 ± 8.8 mV, $p = 0.82$, $t = 2.08$, $df = 20$), quantal content (P) (33.8 ± 6.1 versus 31.7 ± 2.7, $p = 0.37$, $t = 1.76$, $df = 14$), and kinetics of the postsynaptic potentials (Rising phase: 0.7 ± 0.05 ms versus 0.7 ± 0.02 ms, $p = 0.92$, $t = 2.77$, $df = 4$; decay time constant: 1.3 ± 0.18 ms versus 1.1 ± 0.05 ms, $p = 0.43$, $t = 3.18$, $df = 3$) (Q) were not different between fibers from 3 control and 4 *Nmd^{2J}* mice. (R) Estimation of the RRP size by plotting quantal content (y-axis) versus cumulative quantal content (x-axis) and linearly extrapolating the initial decline to the x-axis in two examples. (S) Mean RRP sizes in terminals from 3 control and 4 *Nmd^{2J}* mice were not different (838 ± 125 versus 836 ± 110, $p = 0.99$, $t = 2.1$, $df = 20$). The number of endplates and animals statistically analyzed by Student's unpaired two-tailed *t*-test is put in parentheses. Bars represent mean ± SEM, n.s. = not significant. For statistical analysis see also material and method part.

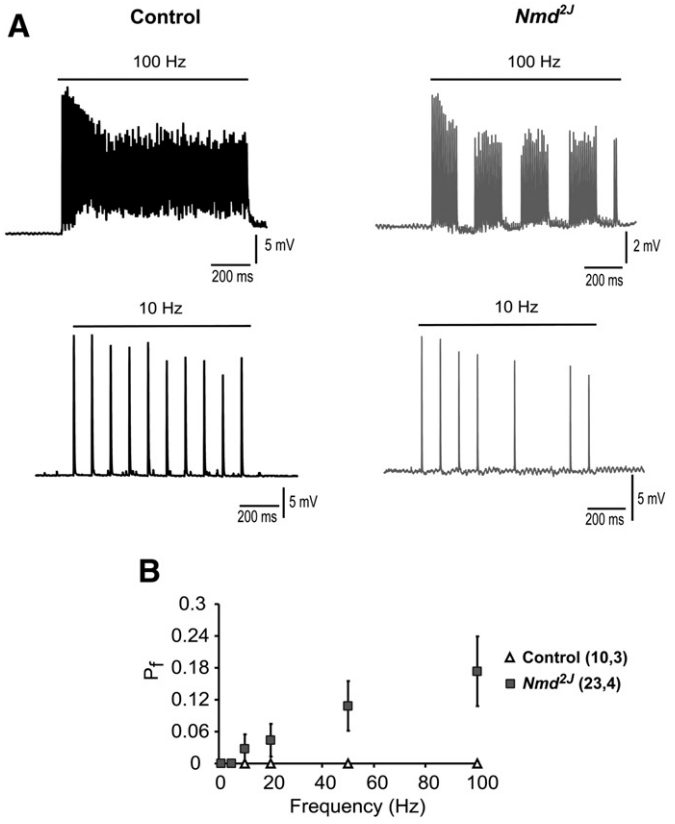

Fig. 7. Repetitive nerve stimulation reveals a defect in nerve-muscle coupling. (A) *Nmd*^{2J} mutant motor terminals exhibit periods of total neurotransmission failure at 100 Hz (upper traces) and 10 Hz (lower traces). (B) Data points show the probability of failure (P_f) at different stimulus frequencies calculated from the electrophysiological recordings. The results show a significant increase of failures at 50 Hz and 100 Hz in *Nmd*^{2J} mice (P_f at 50 Hz: 0 versus 0.11 ± 0.05, $p = 0.03$, $t = 2.01$, $df = 20$; P_f at 100 Hz: 0 versus 0.17 ± 0.08, $p = 0.008$; $t = 2.01$, $df = 22$ for 3 control and 4 *Nmd*^{2J} mice).

forms of SMA (Kong et al., 2009; Park et al., 2010; Ruiz et al., 2010; Torres-Benito et al., 2011). As a third and possibly important difference between SMARD1 and intermediate forms of SMA (Murray et al., 2012), significant signs of sprouting and compensation are observed in *Nmd*^{2J} mice at early stages.

Significant motor axon loss in Nmd^{2J} *mice at early pathological stages*

Nmd^{2J} mice exhibit significant motoneuron loss which corresponds to loss of proximal and distal motor axons at early disease stages when first signs of paralysis appear. This situation is different to that what we and others observed in SMA mouse models (Michaud et al., 2010; Monani et al., 2000, 2003). SMA type I mice die early at birth and appear completely paralyzed, but loss of motoneurons is relatively low in these mice (Monani et al., 2000). Similarly, less severely affected mouse models of SMA type II exhibit motoneuron cell loss not before the mice show signs of paralysis (Michaud et al., 2010; Monani et al., 2003). These observations implicate that disease progression is different between SMARD1 and SMA. In the *Nmd*^{2J} mouse, degenerative signs in the gastrocnemius muscle coexist with motor axon loss and precede degenerative signs in the diaphragm (Fig. 2) which are independent from axon loss of the phrenic nerve (Grohmann et al., 2004). Several reports (Corti et al., 2006; Maddatu et al., 2004, 2005) also support the notion that nerve cell and muscle cell autonomous mechanisms contribute independently to disease phenotype and its progression. For example, the residing cardiomyopathy under a neurogenic overexpression of Ighmbp2 in the *Nmd*^{2J} mouse suggests a neuronal independent disease mechanism in heart (Maddatu et al., 2004). Increasing the number of spinal motoneurons in *Nmd*^{2J} mice by transplanting neuronal stem cells only causes moderate delay in survival time (Corti et al., 2006). And finally, the simultaneous over-expression of Ighmbp2 in *Nmd*^{2J} mice under a neuronal and muscle specific promoter leads to a significant rescue and prolonged survival comparable to control animals (Maddatu et al., 2005).

Our data also confirm that disease progression and the onset of neurogenic versus myopathic paralysis differs between gastrocnemius muscle and the diaphragm, as showed previously (Grohmann et al., 2004). The *Nmd*^{2J} mouse represents a moderate form of SMARD1 with residing full-length Ighmbp2 protein of about 20 to 30% due to an alternative intronic splice site mutation (Cox et al., 1998). The *Nmd*^{2J} phenotype and disease progression resembles that of juvenile SMARD1 patients with IGHMBP2 protein levels ranging from 33 to 40% (Guenther et al., 2009b). Juvenile SMARD1 patients develop diaphragmatic palsy after distal muscular atrophy has been diagnosed (Guenther et al., 2009b). Thus, the data on myogenic impact on the degeneration of the diaphragm in the *Nmd*^{2J} mouse resembles that of the juvenile SMARD1 form, rather than of SMARD1 forms with early onset. Respiratory distress and weakness of limb muscles in infantile SMARD1 patients occur more or less simultaneously (Eckart et al., 2012; Grohmann et al., 2003). However, the question of disease progression and the myogenic and/or neurogenic impact on degeneration of skeletal muscle and diaphragm is still open. Solely Diers et al. (2005) observed motor endplate loss in specimens of post mortem diaphragmatic tissue from infantile SMARD1 patients.

Therefore, our actual data on progression of motoneuron/axon loss and the morphological and functional analysis of the motor endplates in the gastrocnemius muscle from *Nmd*^{2J} mice should be rather discussed for the juvenile SMARD1 form than for infantile SMARD1 form.

Neurotransmission is not affected as long as the NMJs are intact in Nmd^{2J} *mice*

The morphological analysis of neuromuscular endplates in *Nmd*^{2J} mouse mutants at different disease stages revealed that a subpopulation of NMJs is maintained. Postsynapatic structures remain intact as long as they are innervated, and clustering of acetylcholine receptors is even maintained in denervated muscle fibers. Starting from P10 when the mice are phenotypically still unaffected, up to the early symptomatic stages P16 and P21, three different categories of NMJs could be distinguished by confocal and electron-microscopy (Figs. 4, 5): 1) motor endplates with intact innervation and normal synaptic morphology; 2) the fully denervated motor endplate displaying different degrees of postsynaptic degeneration, and 3) a minority of NMJs (2–4%) which exhibited a fragmented presynaptic structure with degenerating axons and invading Schwann cells. Neurofilament inclusions are not detectable in any of these neuromuscular endplates, in contrast to mouse models of spinal muscular atrophy (Cifuentes-Diaz et al., 2002; Park et al., 2010). Schwann cells that invade the synaptic cleft have also been observed in biopsies from SMARD1 patients (Diers et al., 2005). In SMA type II mouse models, the majority of endplates exhibits a fragmented structure at the axon terminals (Kong et al., 2009; Park et al., 2010). Ultrastructural analysis of Smn deficient motor endplates, as well as immunohistochemistry analysis, reveals less vesicles within the presynaptic compartment (Kong et al., 2009; Torres-Benito et al., 2011), which coincides with reduced neurotransmission that is found at all disease stages at neuromuscular junctions (Kong et al., 2009; Ruiz et al., 2010). Similar observations were reported for mouse models for ALS (Amyotrophic Lateral Sclerosis), i.e. *SOD1 G93A* mutant mice (Fischer et al., 2004; Frey et al., 2000; Pun et al., 2006). NMJ loss in *G93A SOD1* mice starts at P50 before loss of motor axons in ventral roots is detectable and clinical signs of disease arise (Fischer et al., 2004; Frey et al., 2000). The dying back process in *SOD1 G93A* mice is accompanied by vesicle stalling (Pun et al., 2006). Loss of synaptic vesicles in axon terminals is not observed in the SMARD1 mouse model.

Motoneuron cell death in other mouse and rat models for monogenetic forms of ALS has been reported i.e. in rodents expressing mutant forms of TDP43 (Stallings et al., 2009; Wils et al., 2010; Wu et al., 2012) and FUS/TLS (Huang et al., 2011; Mitchell et al., 2012). Only for the *FUS/TLS* models a correlation between motoneuron cell death and NMJ loss has been described (Huang et al., 2011; Mitchell et al., 2012). Another mouse model suffering from motoneuron degeneration, but unrelated to known monogenetic forms of human motoneuron disease, the progressive motoneuronopathy *(pmn)* mouse presents also a 'dying back' disease, starting at motor endplates with subsequent axonal degeneration and final loss of motoneuron cell bodies in brain stem and spinal cord (Holtmann et al., 1999; Schmalbruch et al., 1991). Based on these data, we conclude that the mouse model of SMARD1 is different, showing no evidence for a dying back process. Drosophila models of SMA reveal a disease mechanism that primarily affects cholinergic interneurons associated with U12 miss-splicing that is caused by Smn depletion. The aberrant splicing of *Stasimon* leads to reduced excitability of interneurons and motoneuron degeneration appears as a consequence of interneuron dysfunction (Imlach et al., 2012; Lotti et al., 2012). These results also raise questions on whether altered mRNA processing contributes to the pathophysiology of SMARD1 and other forms of motoneuron diseases.

IGHMBP2 is a DNA/RNA helicase, and in this respect similar to Senataxin (SETX). SETX contains a SF1 DNA/RNA helicase domain with an ATP/GTP binding motif essential for DNA unwinding (Chen et al., 2006). Autosomal dominant mutations in *SETX* were identified in a juvenile form of ALS (Chen et al., 2006; Hirano et al., 2011), characterized by limb weakness, muscle wasting and degeneration of motoneurons in brain and spinal cord (Chen et al., 2006; De Jonghe et al., 2002; Rabin et al., 1999). Knockdown of *SETX* in primary neurons leads to axonal growth defects (Vantaggiato et al., 2011). It would be interesting to know whether motoneurons and neuromuscular endplates show similar phenotypes in a Senataxin mutant mouse model, and thus could help to understand whether differences in disease onset and progression correlate with different cellular pathophysiologies between SF1 ATPase/Helicase deficient models, Smn deficient and *TDP43* and *FUS/TLS* mutant models.

The mouse model of SMARD1 used here reveals that motor axon loss does not correspond to neurotransmission defects at the neuromuscular endplate, even at later disease stages.

We have chosen the LAL muscle for this approach because of its convenient accessibility and ideal morphology, due to its sparse layers, in order to avoid false positive or false negative background signals. Muscle fiber degeneration within the LAL muscle was clearly detectable at later stages of the disease (Fig. 6). In contrast, neurotransmission was unaffected with regard to spontaneous release, quantal content, RRP size, and rise and decay time of the EPPs in Nmd^{2J} mice. The detected failures upstream of neurotransmitter release at higher stimuli are most likely caused by defective axonal conduction of action potentials, which in addition indicates a motor axon defect independent from a defective neurotransmission at the endplate. Therefore, it can be concluded that the neurodegenerative process in Nmd^{2J} mice does not predominantly affect the neuromuscular endplate and the neurotransmission machinery, in contrast to other SMA and ALS mouse models, as known so far.

Axon terminals from Nmd^{2J} mice have the potency to sprout

The capability of motor axons to sprout is a mechanism for re-innervating denervated muscle fibers in motoneuron diseases. Investigation of motor axon branching in the gastrocnemius muscle at different disease stages reveals that sprouting apparently occurs at early stages (at P16 and P21) in SMARD1 mice. Our findings are in line with the observation, that motor units with increased size are detectable and functional even at later disease stages (Ruiz et al., 2005). Hypertrophic muscle fibers are not detectable in SMARD1 patients. These compensatory mechanisms appear much more pronounced than in most common severe and intermediate forms of SMA. Axonal sprouting is generally not observed in severe forms of SMA in patients (Korinthenberg et al., 1997) and SMA type I and intermediated forms of SMA mouse models (Monani et al., 2000; Murray et al., 2012). However, in some infantile SMARD1 patients, defective collateral reinnervation has also been described (Diers et al., 2005). The Nmd^{2J} mouse is a model for a moderate disease progression of SMARD1. The long preservation of morphology and function of NMJs facilitates the initiation of re-innervation by sprouting and the establishment of functional endplates. In this situation of slow progression, neurotrophic factors from residual Schwann cells at the nerve terminals, which are intact in the Nmd^{2J} mouse, or from the postsynapse could support maintenance of axons and muscle innervation, as it was described for the SMA type III mouse (Simon et al., 2010).

The maintenance of a functional intact NMJ even at later disease stages and the capability to sprout could be one option in order to delay muscular atrophy. Sprouting in SMA type III mice is triggered by the ciliary neurotrophic factor (CNTF) (Simon et al., 2010). Thus, endogenous CNTF and stimulation of release of this neurotrophic factor could be one possible therapeutic approach. It has been shown that CNTF application in the *pmn* mouse and the SOD1 model for FALS extends life span corresponding to reduction in motoneuron loss (Giess et al., 2002; Sendtner et al., 1992). Previously we could demonstrate in the *pmn* mouse that an IGF-I variant with a site specific addition of polyethylene glycol (pIGF-1) shows myogenic and neurogenic potential including extended life span and reduced motoneuron cell body and motor axon loss in the phrenic nerve (Jablonka et al., 2011). On account of these findings similar approaches in the Nmd^{2J} mouse are conceivable.

Conclusion

Our studies on the Nmd^{2J} mouse, a model for the juvenile form of SMARD1 reveals a disease progression which differs from disease progression in SMA type I and II mice. Motor axon degeneration precedes fiber atrophy in the gastrocnemius muscle and is detectable along the whole spinal cord-muscle axis. Morphologically unaffected NMJs and intact neurotransmission in individual motoneurons indicate a disease mechanism, which does not primarily affect the neuromuscular endplate as it is described for SMA mouse models. The capacity for sprouting is high in Nmd^{2J} mice and thus could be a start point for the identification of survival supporting mechanisms in Nmd^{2J} motoneurons.

Acknowledgments

This work was supported by the Deutsche Forschungsgemeinsschaft (SFB 581/B24, B18 and Z3), Fundació Marató *TV3* (grant 062331), FIS-PS09/01267, and CIBERNED. We thank Michael Sendtner for helpful discussions concerning the manuscript; Victor Buterus and Regine Sendtner for the stock breeding; Karin Reinfurt-Gehm and Sieglinde Schenk for their help on ultrastructural histology of the motor endplate.

No conflict of interest exists.

References

Bertini, E., et al., 1989. Distal infantile spinal muscular atrophy associated with paralysis of the diaphragm: a variant of infantile spinal muscular atrophy. Am. J. Med. Genet. 33, 328–335.

Brook, G.A., Duchen, L.W., 1990. End-plates, transmission and contractile characteristics of muscles without spindles in the hereditary sensory neuropathy of the Sprawling mouse. Brain 113, 867–891.

Cardasis, C.A., Padykula, H., 1981. Ultrastructural evidence indicating reorganization at the neuromuscular junction in the normal rat soleus muscle. Anat. Rec. 200, 41–59.

Caroni, P., 1997. Overexpression of growth-associated proteins in the neurons of adult transgenic mice. J. Neurosci. Methods 71, 3–9.

Chen, Y.Z., et al., 2006. Senataxin, the yeast Sen1p orthologue: characterization of a unique protein in which recessive mutations cause ataxia and dominant mutations cause motor neuron disease. Neurobiol. Dis. 23, 97–108.

Cifuentes-Diaz, C., et al., 2002. Neurofilament accumulation at the motor endplate and lack of axonal sprouting in a spinal muscular atrophy mouse model. Hum. Mol. Genet. 11, 1439–1447.
Corti, S., et al., 2006. Transplanted ALDHhiSSClo neural stem cells generate motor neurons and delay disease progression of nmd mice, an animal model of SMARD1. Hum. Mol. Genet. 15, 167–187.
Cox, G.A., et al., 1998. Identification of the mouse neuromuscular degeneration gene and mapping of a second site suppressor allele. Neuron 21, 1327–1337.
De Jonghe, P., et al., 2002. Autosomal dominant juvenile amyotrophic lateral sclerosis and distal hereditary motor neuronopathy with pyramidal tract signs: synonyms for the same disorder? Brain 125, 1320–1325.
Diers, A., et al., 2005. The ultrastructure of peripheral nerve, motor end-plate and skeletal muscle in patients suffering from spinal muscular atrophy with respiratory distress type 1 (SMARD1). Acta Neuropathol. 110, 289–297.
Eckart, M., et al., 2012. The natural course of infantile spinal muscular atrophy with respiratory distress type 1 (SMARD1). Pediatrics 129, e148–e156.
Elmqvist, D., Quastel, D.M., 1965. A quantitative study of end-plate potentials in isolated human muscle. J. Physiol. 178, 505–529.
Feng, G., et al., 2000. Imaging neuronal subsets in transgenic mice expressing multiple spectral variants of GFP. Neuron 28, 41–51.
Fischer, L.R., et al., 2004. Amytrophic lateral sclerosis is a distal axonopathy: evidence in mice and man. Exp. Neurol. 185, 232–240.
Frey, D., et al., 2000. Early and selective loss of neuromuscular synapse subtypes with low sprouting competence in motoneuron diseases. J. Neurosci. 20, 2534–2542.
Giess, R., et al., 2002. Early onset of severe familial amyotrophic lateral sclerosis with a SOD-1 mutation: potential impact of CNTF as a candidate modifier gene. Am. J. Hum. Genet. 70, 1277–1286.
Grohmann, K., et al., 1999. Diaphragmatic spinal muscular atrophy with respiratory distress is heterogeneous, and one form is linked to chromosome 11q13-q21. Am. J. Hum. Genet. 65, 1459–1462.
Grohmann, K., et al., 2001. Mutations in the gene encoding immunoglobulin mu-binding protein 2 cause spinal muscular atrophy with respiratory distress type 1. Nat. Genet. 29, 75–77.
Grohmann, K., et al., 2003. Infantile spinal muscular atrophy with respiratory distress type 1 (SMARD1). Ann. Neurol. 54, 719–724.
Grohmann, K., et al., 2004. Characterization of Ighmbp2 in motor neurons and implications for the pathomechanism in a mouse model of human spinal muscular atrophy with respiratory distress type 1 (SMARD1). Hum. Mol. Genet. 13, 2031–2042.
Guenther, U.P., et al., 2007. Clinical and mutational profile in spinal muscular atrophy with respiratory distress (SMARD): defining novel phenotypes through hierarchical cluster analysis. Hum. Mutat. 28, 808–815.
Guenther, U.P., et al., 2009a. IGHMBP2 is a ribosome-associated helicase inactive in the neuromuscular disorder distal SMA type 1 (DSMA1). Hum. Mol. Genet. 18, 1288–1300.
Guenther, U.P., et al., 2009b. Clinical variability in distal spinal muscular atrophy type 1 (DSMA1): determination of steady-state IGHMBP2 protein levels in five patients with infantile and juvenile disease. J. Mol. Med. 87, 31–41.
Hirano, M., et al., 2011. Senataxin mutations and amyotrophic lateral sclerosis. Amyotroph. Lateral Scler. 12, 223–227.
Holtmann, B., et al., 1999. Comparative analysis of motoneuron loss and functional deficits in PMN mice: implications for human motoneuron disease. J. Neurol. Sci. 169, 140–147.
Huang, C., et al., 2011. FUS transgenic rats develop the phenotypes of amyotrophic lateral sclerosis and frontotemporal lobar degeneration. PLoS Genet. 7, e1002011.
Imlach, W.L., et al., 2012. SMN is required for sensory-motor circuit function in Drosophila. Cell 151, 427–439.
Jablonka, S., et al., 2011. Therapeutic effects of PEGylated insulin-like growth factor I in the pmn mouse model of motoneuron disease. Exp. Neurol. 232, 261–269.
Jankowsky, E., 2011. RNA helicases at work: binding and rearranging. Trends Biochem. Sci. 36, 19–29.
Kong, L., et al., 2009. Impaired synaptic vesicle release and immaturity of neuromuscular junctions in spinal muscular atrophy mice. J. Neurosci. 29, 842–851.
Korinthenberg, R., et al., 1997. Congenital axonal neuropathy caused by deletions in the spinal muscular atrophy region. Ann. Neurol. 42, 364–368.
Lotti, F., et al., 2012. An SMN-dependent U12 splicing event essential for motor circuit function. Cell 151, 440–454.
Maddatu, T.P., et al., 2004. Transgenic rescue of neurogenic atrophy in the nmd mouse reveals a role for Ighmbp2 in dilated cardiomyopathy. Hum. Mol. Genet. 13, 1105–1115.
Maddatu, T.P., et al., 2005. Dilated cardiomyopathy in the nmd mouse: transgenic rescue and QTLs that improve cardiac function and survival. Hum. Mol. Genet. 14, 3179–3189.
McLachlan, E.M., Martin, A.R., 1981. Non-linear summation of end-plate potentials in the frog and mouse. J. Physiol. 311, 307–324.
Michaud, M., et al., 2010. Neuromuscular defects and breathing disorders in a new mouse model of spinal muscular atrophy. Neurobiol. Dis. 38, 125–135.
Mitchell, J.C., et al., 2012. Overexpression of human wild-type FUS causes progressive motor neuron degeneration in an age- and dose-dependent fashion. Acta Neuropathol. (Sep. 9). http://dx.doi.org/10.1007/s00401-012-1043-z.
Monani, U.R., et al., 2000. The human centromeric survival motor neuron gene (SMN2) rescues embryonic lethality in Smn(−/−) mice and results in a mouse with spinal muscular atrophy. Hum. Mol. Genet. 9, 333–339.
Monani, U.R., et al., 2003. A transgene carrying an A2G missense mutation in the SMN gene modulates phenotypic severity in mice with severe (type I) spinal muscular atrophy. J. Cell Biol. 160, 41–52.
Murray, L.M., et al., 2012. Defects in neuromuscular junction remodelling in the $Smn^{2B/-}$ mouse model of spinal muscular atrophy. Neurobiol. Dis. 49C, 57–67 (Aug. 30).
Noakes, P.G., et al., 1995. Aberrant differentiation of neuromuscular junctions in mice lacking s-laminin/laminin beta 2. Nature 374, 258–262.
Park, G.H., et al., 2010. Reduced survival of motor neuron (SMN) protein in motor neuronal progenitors functions cell autonomously to cause spinal muscular atrophy in model mice expressing the human centromeric (SMN2) gene. J. Neurosci. 30, 12005–12019.
Pun, S., et al., 2006. Selective vulnerability and pruning of phasic motoneuron axons in motoneuron disease alleviated by CNTF. Nat. Neurosci. 9, 408–419.
Rabin, B.A., et al., 1999. Autosomal dominant juvenile amyotrophic lateral sclerosis. Brain 122, 1539–1550.
Reynolds, E.S., 1963. The use of lead citrate at high pH as an electron opaque stain in electron microscopy. J. Cell Biol. 17, 208–212.
Rudnik-Schoneborn, S., et al., 2004. Long-term observations of patients with infantile spinal muscular atrophy with respiratory distress type 1 (SMARD1). Neuropediatrics 35, 174–182.
Ruiz, R., et al., 2005. Treatment with trkC agonist antibodies delays disease progression in neuromuscular degeneration (nmd) mice. Hum. Mol. Genet. 14, 1825–1837.
Ruiz, R., et al., 2008. Cysteine string protein-alpha is essential for the high calcium sensitivity of exocytosis in a vertebrate synapse. Eur. J. Neurosci. 27, 3118–3131.
Ruiz, R., et al., 2010. Altered intracellular Ca2+ homeostasis in nerve terminals of severe spinal muscular atrophy mice. J. Neurosci. 30, 849–857.
Ruiz, R., et al., 2011. Active zones and the readily releasable pool of synaptic vesicles at the neuromuscular junction of the mouse. J. Neurosci. 31, 2000–2008.
Schiaffino, S., et al., 1988. Embryonic and neonatal myosin heavy chain in denervated and paralyzed rat skeletal muscle. Dev. Biol. 127, 1–11.
Schmalbruch, H., et al., 1991. A new mouse mutant with progressive motor neuronopathy. J. Neuropathol. Exp. Neurol. 50, 192–204.
Sendtner, M., et al., 1992. Ciliary neurotrophic factor prevents degeneration of motor neurons in mouse mutant progressive motor neuronopathy. Nature 358, 502–504.
Simon, C.M., et al., 2010. Ciliary neurotrophic factor-induced sprouting preserves motor function in a mouse model of mild spinal muscular atrophy. Hum. Mol. Genet. 19, 973–986.
Stallings, N.R., et al., 2009. Generation and characterization of wild-type and mutant TDP-43 transgenic mice. Abstract Book.Society For Neuroscience.
Torres-Benito, L., et al., 2011. SMN requirement for synaptic vesicle, active zone and microtubule postnatal organization in motor nerve terminals. PLoS One 6 (10), e26164 (Epub 2011 Oct. 12).
Vantaggiato, C., et al., 2011. Senataxin modulates neurite growth through fibroblast growth factor 8 signalling. Brain 134, 1808–1828.
Wils, H., et al., 2010. TDP-43 transgenic mice develop spastic paralysis and neuronal inclusions characteristic of ALS and frontotemporal lobar degeneration. Proc. Natl. Acad. Sci. U. S. A. 107, 3858–3863.
Wu, L.S., et al., 2012. Targeted depletion of TDP-43 expression in the spinal cord motor neurons leads to the development of amyotrophic lateral sclerosis-like phenotypes in mice. J. Biol. Chem. 287, 27335–27344.